

# FeSe<sub>2</sub> films with controllable morphologies as efficient counter electrodes for dye-sensitized solar cells†

Cite this: *Chem. Commun.*, 2014, 50, 2618Received 3rd December 2013,  
Accepted 10th January 2014

DOI: 10.1039/c3cc49175g

www.rsc.org/chemcomm

Wenjun Wang,<sup>a</sup> Xu Pan,<sup>\*a</sup> Weiqing Liu,<sup>a</sup> Bing Zhang,<sup>b</sup> Haiwei Chen,<sup>a</sup> Xiaqin Fang,<sup>a</sup> Jianxi Yao<sup>b</sup> and Songyuan Dai<sup>\*ab</sup>

**The FeSe<sub>2</sub> films with controllable morphologies (including 3D flower-like and sphere-shaped) have been applied as the counter electrodes (CEs) for dye-sensitized solar cells (DSSCs). It is found that 3D flower-like FeSe<sub>2</sub> CEs perform comparably to conventional platinum CEs (power conversion efficiencies of 8.00 and 7.87%, respectively).**

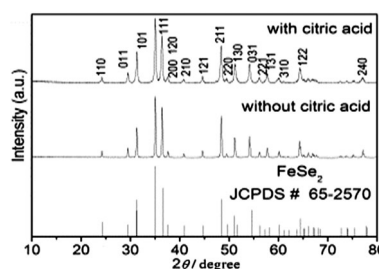
Dye-sensitized solar cells (DSSCs) are promising alternatives to conventional solid-state photovoltaic devices based on materials such as Si, CdTe and CuIn<sub>1-x</sub>Ga<sub>x</sub>Se<sub>2</sub>, owing to their low cost, ease of production and high efficiency.<sup>1</sup> In general, a typical DSSC usually comprises three main components: a dye-sensitized porous nanocrystalline titanium dioxide (TiO<sub>2</sub>) film as the photoanode, an electrolyte traditionally containing an iodide/triiodide (I<sup>-</sup>/I<sub>3</sub><sup>-</sup>) redox couple and a counter electrode (CE).

As a crucial component, CE plays an important role in the performance of a DSSC in that it collects electrons from external circuit and fulfills electron transfer from the CE interface to the electrolyte by catalyzing the reduction of I<sub>3</sub><sup>-</sup> to I<sup>-</sup>. Usually, fluorine doped tin oxide (FTO) glass loaded with noble metal platinum (Pt) is the preferred material for the CE due to its superior conductivity, electrocatalytic activity and stability.<sup>2</sup> However, in view of the low abundance and high cost of platinum, much incentive exists in developing other cost-effective alternatives for Pt. For instance, carbon materials,<sup>3</sup> conducting polymers<sup>4</sup> and inorganic compounds<sup>5,6</sup> have been utilized as CEs in DSSCs. In particular, some metal chalcogenides among these Pt-free electrocatalysts have been shown to be quite effective and have exceeded the performance of Pt.<sup>7-10</sup> As another compound in the metal chalcogenide series, iron diselenide (FeSe<sub>2</sub>) is an important VIII-VI transition metal selenide semiconductor and has drawn enormous attention owing to its unusual structure and electronic properties, as well as the opportunity it offers to engineer

special shapes for application in the development of advanced functional devices. In recent years, much effort has been devoted to the synthesis of FeSe<sub>2</sub> films, low-dimensional FeSe<sub>2</sub> micro/nanostructures and anisotropic three-dimensional (3D) FeSe<sub>2</sub> nanostructures. However, to the best of our knowledge, no research on the use of FeSe<sub>2</sub> as CEs in DSSCs has been reported so far.

Herein, as the electrocatalytic activity may depend on the morphology, we have prepared the FeSe<sub>2</sub> films with controllable morphologies, including 3D flower-like FeSe<sub>2</sub> assembled with nano/microrods (F<sub>r</sub>) and sphere-shaped FeSe<sub>2</sub> assembled with sphere-shaped particles (F<sub>s</sub>), *via* a facile hydrothermal synthetic approach, and used them as Pt-free electrocatalysts for DSSCs, respectively. Electrochemical results of the F<sub>r</sub> CE showed Pt-like catalytic activity for triiodide reduction, surpassing that of the F<sub>s</sub> CE. As a result, the power conversion efficiency ( $\eta$ ) of the DSSC with the F<sub>r</sub> CE was 8.00%, which was comparable to that of the Pt CE (7.87%), while the  $\eta$  of the F<sub>s</sub> CE was 7.38%. Details of the fabrication method are shown in the experimental section of the ESI.†

The crystallographic structures of the as-synthesized FeSe<sub>2</sub> products were characterized by X-ray diffraction (XRD). From the XRD patterns (Fig. 1), all diffraction peaks of F<sub>r</sub> and F<sub>s</sub> can be readily indexed to an orthorhombic phase of FeSe<sub>2</sub> (JCPDS No. 65-2570). The morphologies of the FeSe<sub>2</sub> samples (F<sub>r</sub> and F<sub>s</sub>) were observed using typical scanning electron microscopy (SEM) and transmission electron microscopy (TEM). As shown in Fig. 2a, the as-obtained F<sub>r</sub> CE in the reaction system without citric acid consists almost entirely of the flower-like FeSe<sub>2</sub> assembled with micro/nanorods with an

Fig. 1 XRD patterns of the as-synthesized FeSe<sub>2</sub> products.

<sup>a</sup> Key lab of Novel Thin Film Solar Cells, Institute of Plasma Physics, Chinese Academy of Sciences, Hefei, PR China. E-mail: sydai@ipp.ac.cn, mars\_dark@hotmail.com; Fax: +86 (0)551 5591377; Tel: +86 (0)551 5591377

<sup>b</sup> State Key Laboratory of Alternate Electrical Power System with Renewable Energy Sources, North China Electric Power University, Beijing 102206, China

† Electronic supplementary information (ESI) available: Full experimental procedures. See DOI: 10.1039/c3cc49175g

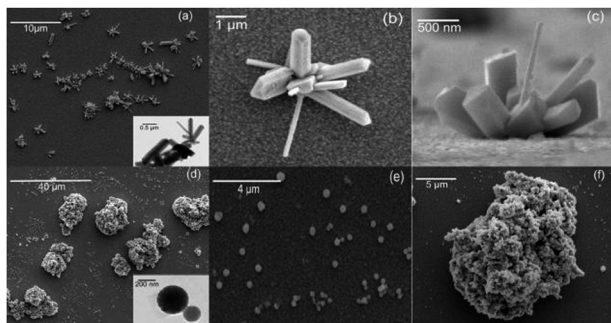


Fig. 2 (a) Low-, (b) high-magnification and (c) cross-section SEM images of  $F_r$  grown *in situ* on the FTO glass. The inset shows the TEM image of  $F_r$ . (d) Low and (e, f) high-magnification SEM images of  $F_s$  grown *in situ* on the FTO glass. The inset shows the TEM image of  $F_s$ .

average diameter of 0.5–3  $\mu\text{m}$ . Only a small portion of single micro/nanorods can be found. As shown in Fig. 2(b) and (c), the 3D flower-like microconstruction is composed of many 1-dimensional subunits (micro/nanorods) that connect with each other by self-assembly. The inset shows the TEM image of  $F_r$ . Fig. 2d shows the SEM image of the as-obtained  $F_s$  CE in the same reaction system with additional citric acid. The surface is partially covered with single relatively uniform sphere-shaped particles (Fig. 2e). Meanwhile, other parts of the film have large near-spherical particles. The sizes of the large near-spherical particles are found to be in micrometer-scale. As can be seen at higher magnification (Fig. 2f), the large near-spherical particles are composed of lots of nanoparticles. The inset of Fig. 2d shows the TEM image of single sphere-shaped particles with a mean size of 200–400 nm.

The performances of the DSSCs with  $F_r$  and  $F_s$  CEs were studied in comparison to that of the DSSC with the Pt CE. The photocurrent–voltage ( $I$ – $V$ ) curves of the DSSCs applying  $F_r$ ,  $F_s$  and Pt CEs are shown in Fig. 3 (under simulated solar light illumination of  $100 \text{ mW cm}^{-2}$ ). The corresponding photovoltaic parameters are summarized in Table 1. As shown in Table 1, when the  $F_r$  was used as the counter electrode, the DSSC exhibits a short-circuit current ( $J_{sc}$ ) of  $14.93 \text{ mA cm}^{-2}$ , an open-circuit voltage ( $V_{oc}$ ) of 744 mV, a fill factor (FF) of 0.721 and an  $\eta$  of 8.00%. The DSSC with the Pt CE, on the contrary, renders a  $J_{sc}$  of  $15.13 \text{ mA cm}^{-2}$ , a  $V_{oc}$  of 741 mV, a FF of 0.702 and an  $\eta$  of 7.87%. The  $F_r$ -based cells showed a comparable, even slightly higher,  $\eta$  than Pt, which is mainly attributed to the slight improvement in the FF. Meanwhile, the  $\eta$  of 7.38% has been obtained by the DSSCs applying  $F_s$  CEs, indicating a poorer catalytic activity for the reduction of  $\text{I}_3^-$ . The incident photon-to-current conversion efficiency (IPCE) spectra of these DSSCs were also collected (see ESI†).

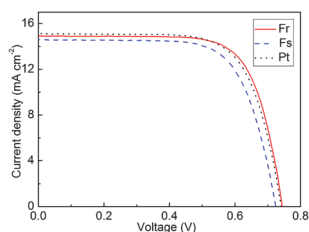


Fig. 3  $I$ – $V$  curves of DSSCs with  $F_r$ ,  $F_s$  and Pt electrodes.

Table 1 Photovoltaic and EIS parameters of the DSSCs with different CEs

CEs	$V_{oc}/\text{mV}$	$J_{sc}/\text{mA cm}^{-2}$	FF	$\eta/\%$	$R_s/\Omega \text{ cm}^2$	$R_{ct}/\Omega \text{ cm}^2$	$Z_N/\Omega \text{ cm}^2$	$E_{pp}/\text{mV}$
$F_r$	744	14.93	0.721	8.00	16.82	0.53	0.43	252
$F_s$	724	14.60	0.698	7.38	27.05	0.96	0.79	302
Pt	741	15.13	0.702	7.87	17.01	0.78	0.59	262

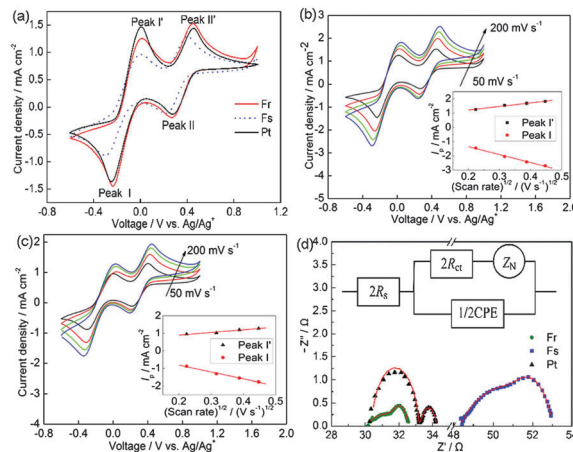


Fig. 4 (a) Cyclic voltammograms for  $F_r$ ,  $F_s$  and Pt CEs obtained at a scan rate of  $50 \text{ mV s}^{-1}$ . (b, c) CV curves of the  $F_r$  and  $F_s$  CEs at various scan rates. The inset shows the redox peak current of eqn (1) as a function of scan rate. (d) Nyquist plots obtained by EIS analysis of the symmetrical cells. The inset gives the equivalent circuit.

To investigate the reaction kinetics of various electrodes in the  $\text{I}^-/\text{I}_3^-$  electrochemical system, cyclic voltammetry (CV) was carried out in a three-electrode system. Fig. 4(a) shows the CV curves of the  $F_r$ ,  $F_s$  and Pt CEs, respectively. Two pairs of redox peaks (peak I/peak I' and peak II/peak II') are observed for all of the materials. The left redox peaks correspond to eqn (1) and the right ones correspond to eqn (2)<sup>11,12</sup>



Since the counter electrode of a DSSC is responsible for catalyzing the reduction of  $\text{I}_3^-$  to  $\text{I}^-$ , the characteristics of peak I and peak I' are the focus of our analysis. The peak current and the peak-to-peak separation ( $E_{pp}$ ), which is negatively correlated with the standard electrochemical rate constant of the redox reaction, are two critical parameters for comparing electrocatalytic activities of different CEs.<sup>13</sup>

As shown in Fig. 4(a), the lower  $E_{pp}$  and higher current densities of the  $F_r$  electrode indicate that  $F_r$  produces higher reversibility of the  $\text{I}_3^-/\text{I}^-$  redox reaction and remarkable electrocatalytic activity for  $\text{I}_3^-$  reduction, even better than Pt, which is advantageous for the application of the  $F_r$  electrode as an efficient CE in DSSCs. Meanwhile, the lower peak current densities and larger  $E_{pp}$  of the  $F_s$  electrode reveal that the electrocatalytic activity of the  $F_s$  electrode is inferior to that of  $F_r$  and Pt electrodes. The conclusion from the CV data is consistent with previous energy conversion efficiency results. The  $\eta$  of the  $F_s$ -based DSSCs are lower than those of  $F_r$  and Pt-based DSSCs, which stems from the inferior electrocatalytic ability of the  $F_s$  electrodes.

Fig. 4(b) and (c) represent the typical CV curves of  $F_r$  and  $F_s$  electrodes in the  $I^-/I_3^-$  system with different scan rates. As shown in Fig. 4(b) and (c), the peak current densities ( $I_p$ ) changed with the scan rate. Also, the cathodic peaks gradually and regularly shifted negatively, and the corresponding anodic peaks shifted positively upon increasing the scan rate. The inset of Fig. 4(b) and (c) illustrates a linear relationship between the redox peak current density and the square root of scan rates. According to the Langmuir isotherms principle, this linear relationship indicates the diffusion limitation of the redox reactions (eqn (1)) on the surface of  $F_r$  and  $F_s$  CE. This phenomenon also shows that the adsorption of iodide species is little affected by the redox reaction on the surface of  $F_r$  and  $F_s$  CEs and there is no specific interaction between the  $I^-/I_3^-$  redox couple and  $F_r$  and  $F_s$  CEs as is the case of the Pt CE.<sup>15,16</sup>

To further elucidate the electrocatalytic activity of the  $FeSe_2$  CEs in the reduction of  $I_3^-$  ions, electrochemical impedance spectroscopy (EIS) was conducted on the symmetrical  $F_r-F_r$ ,  $F_s-F_s$  and Pt-Pt electrochemical cells. Fig. 4(d) shows the Nyquist plots obtained by the EIS analysis of symmetric cells and the equivalent circuit diagram used for the simulation. Generally, the high-frequency intercepts on the real axis represent the series resistance ( $R_s$ ), which is mainly composed of the bulk resistance of CE materials, resistance of FTO glass substrates, contact resistance, etc. The high frequency semicircle indicates the electrochemical charge transfer resistance ( $R_{ct}$ ) at the interface of CE/electrolyte for  $I_3^-$  reduction and the corresponding constant phase element (CPE) describing deviation from the ideal capacitance, due to the electrode roughness, whereas the low frequency semicircle indicates the Nernst diffusion-limited impedance ( $Z_n$ ) of the  $I^-/I_3^-$  redox species in the electrolyte.<sup>16</sup> The Nyquist plots were fitted and the impedance parameters of various electrodes obtained by fitting are shown in Table 1. The  $F_r$  CE possessed the lowest  $R_{ct}$  (0.53  $\Omega$   $cm^2$ ), so it had a relatively high catalytic activity. The conclusions derived from the EIS and CV data are consistent. Furthermore, previous analyses have indicated that the total series resistance ( $R_{series}$ ) of solar cells strongly influences the FF and  $\eta$ .<sup>16,17</sup> In DSSCs, the  $R_{series}$  is mainly related to  $R_s$ ,  $R_{ct}$ , the diffusion impedance of  $I_3^-$  ions in the electrolyte and the electron transfer at the  $TiO_2$ /dye/electrolyte interface.<sup>17</sup> The lowest  $R_{ct}$ ,  $R_s$  and  $Z_n$  of the  $F_r$  CE resulted in the minimum series resistance, and hence the  $F_r$  based device showed a corresponding improvement in the FF and  $\eta$ . Meanwhile, the  $R_s$  of  $F_s$  increased significantly compared to  $F_r$ , which also resulted in a lower electrocatalytic activity.

In addition, although the exact reason for the influence of morphology on the performance of  $FeSe_2$  CEs is still unclear, the following points may be noted. In principle, the prerequisite for triiodide reduction is the adsorption of acceptor-like species (such as  $I_2$  and  $I_3^-$ ) at active sites of semiconductor catalysts ( $FeSe_2$ ) through charge-transfer chemisorption.<sup>16,18</sup> Therefore, the performance of  $FeSe_2$  CEs is sensitive to their surface structure. The 3D flower-like morphology may improve the total surface area exposed to the electrolyte, which may facilitate the triiodide reduction reaction on the  $F_r$  CE. In contrast, the  $F_s$  CE consists of many large near-spherical particles, which may result in an increase in the  $R_s$  as well as the average current carrier transport length before reaching the site for triiodide reduction.<sup>19</sup>

Meanwhile, with irregular surfaces, the electrons or holes must move through many interfaces before they can meet and recombine with each other,<sup>10</sup> which may result in the inferior electrocatalytic activity of  $F_s$ . However, the  $F_s$  CE is also covered with single sphere-shaped particles that may be active sites to improve the electrocatalytic activity. As a consequence, the  $F_s$  CE still exhibits good electrocatalytic activity.

In conclusion, we have shown that  $FeSe_2$  films with controllable morphologies (including 3D flower-like and sphere-shaped) can be used as electrocatalysts for triiodide reduction in DSSCs. The  $F_r$  CE has been successfully demonstrated to be an efficient electrocatalyst with low charge-transfer resistance ( $R_{ct}$ ) and fast reaction rates for the reduction of  $I_3^-$  ions, even slightly superior to Pt. As a consequence, the DSSC with the 3D flower-like  $FeSe_2$  CE shows an  $\eta$  of 8.00%, slightly higher than that of the DSSC using a Pt CE (7.87%). In contrast, the  $F_s$  CE is inferior to the  $F_r$  CE. Furthermore, the simple preparation procedure and inexpensive cost properties of the  $FeSe_2$  CE allow the development of a high-performance  $FeSe_2$  CE to replace the expensive Pt CE catalyst in large-scale industrial DSSC production.

This work was financially supported by the National Basic Research Program of China under Grant No. 2011CBA00700, the National High Technology Research and Development Program of China under Grant No. 2010AA050510, and the National Natural Science Foundation of China under Grant No. 21273242, 21173227, 21103197.

## Notes and references

- 1 M. Gratzel, *Acc. Chem. Res.*, 2009, **42**, 1788–1798.
- 2 N. Papageorgiou, W. F. Maier and M. Gratzel, *J. Electrochem. Soc.*, 1997, **144**, 876–884.
- 3 K. S. Lee, W. J. Lee, N. G. Park, S. O. Kim and J. H. Park, *Chem. Commun.*, 2011, **47**, 4264–4266.
- 4 S. Ahmad, J. H. Yum, X. X. Zhang, M. Gratzel, H. J. Butt and M. K. Nazeeruddin, *J. Mater. Chem.*, 2010, **20**, 1654–1658.
- 5 X. J. Zheng, J. H. Guo, Y. T. Shi, F. Q. Xiong, W. H. Zhang, T. L. Ma and C. Li, *Chem. Commun.*, 2013, **49**, 9645–9647.
- 6 M. X. Wu, X. Lin, Y. D. Wang, L. Wang, W. Guo, D. D. Qu, X. J. Peng, A. Hagfeldt, M. Gratzel and T. L. Ma, *J. Am. Chem. Soc.*, 2012, **134**, 3419–3428.
- 7 F. Gong, X. Xu, Z. Q. Li, G. Zhou and Z. S. Wang, *Chem. Commun.*, 2013, **49**, 1437–1439.
- 8 F. Gong, H. Wang, X. Xu, G. Zhou and Z. S. Wang, *J. Am. Chem. Soc.*, 2012, **134**, 10953–10958.
- 9 M. K. Wang, A. M. Anghel, B. Marsan, N. L. C. Ha, N. Pootrakulchote, S. M. Zakeeruddin and M. Gratzel, *J. Am. Chem. Soc.*, 2009, **131**, 15976–15977.
- 10 Y. C. Wang, D. Y. Wang, Y. T. Jiang, H. A. Chen, C. C. Chen, K. C. Ho, H. L. Chou and C. W. Chen, *Angew. Chem., Int. Ed.*, 2013, **52**, 6694–6698.
- 11 A. I. Popov and D. H. Geske, *J. Am. Chem. Soc.*, 1958, **80**, 1340–1352.
- 12 G. Boschloo and A. Hagfeldt, *Acc. Chem. Res.*, 2009, **42**, 1819–1826.
- 13 J. D. Roy-Mayhew, D. J. Bozym, C. Punckt and I. A. Aksay, *ACS Nano*, 2010, **4**, 6203–6211.
- 14 S. Biallozor and A. Kupniewska, *Electrochem. Commun.*, 2000, **2**, 480–486.
- 15 Y. Saito, W. Kubo, T. Kitamura, Y. Wada and S. Yanagida, *J. Photochem. Photobiol., A*, 2004, **164**, 153–157.
- 16 A. Hauch and A. Georg, *Electrochim. Acta*, 2001, **46**, 3457–3466.
- 17 N. Koide, A. Islam, Y. Chiba and L. Y. Han, *J. Photochem. Photobiol., A*, 2006, **182**, 296–305.
- 18 Y. Hou, D. Wang, X. H. Yang, W. Q. Fang, B. Zhang, H. F. Wang, G. Z. Lu, P. Hu, H. J. Zhao and H. G. Yang, *Nat. Commun.*, 2013, **4**, 1583.
- 19 T. N. Murakami, S. Ito, Q. Wang, M. K. Nazeeruddin, T. Bessho, I. Cesar, P. Liska, R. Humphry-Baker, P. Comte, P. Pechy and M. Gratzel, *J. Electrochem. Soc.*, 2006, **153**, A2255–A2261.